nature communications

Article

https://doi.org/10.1038/s41467-026-68759-9

Asymmetric Pt_1C_3-$Pt_1O_1C_3$ catalytic pairs for efficient transfer hydrogenation of azobenzene

Received: 22 April 2025

Accepted: 15 January 2026

Published online: 02 February 2026

Check for updates

Yiyun Fang[1,9] ✉, Wen Zhao[1,9], Zhilin Xing[1,9], Cheng Chen[2,9], Xin Zhou[3,9], Congcong Cui[1], Xuchao Wang[1], Siming Zheng[1], Qiyuan Liu[4], Diandong Lv[1], Siqi Li[1], Zhaohang Chen[1], Zi-Qiang Rong[1] ✉, Na Guo[5,6] ✉, Xinzhe Li[4] ✉ & Bin Liu[7,8] ✉

Atomic catalytic pairs (CPs) have shown great promise in driving multi-step catalytic transformations, yet the influence of spatial arrangement and coordination asymmetry on homonuclear CPs remain poorly understood. Herein, we construct atomically dispersed homonuclear Pt_1-Pt_1 CPs with asymmetric Pt_1C_3-$Pt_1O_1C_3$ coordination anchored on reduced graphene oxide. By precisely tuning the spacing between the adjacent Pt_1C_3-$Pt_1O_1C_3$ CPs to approximately 5.3 Å, the catalyst achieves an exceptional turnover frequency of 27,218 h^{-1} for transfer hydrogenation of azobenzene via ammonia-borane hydrolysis, surpassing benchmarking catalysts by more than an order of magnitude. The Pt_1C_3-$Pt_1O_1C_3$ CPs separated by 5.3 Å can facilitate co-adsorption of sterically hindered intermediates and at the same time the asymmetric Pt_1C_3-$Pt_1O_1C_3$ coordination enables facile hydrogen shuttling and barrier-suppressed hydrogenation. These synergistic effects enhance the overall azobenzene hydrogenation efficiency. Our findings uncover a fundamental spatial design principle for atomically precise homonuclear asymmetric CPs, offering new opportunities for sustainable and efficient fine chemical synthesis.

Catalysis lies at the heart of transformative innovations in sustainable chemical synthesis and energy conversion technologies. Single-atom catalysts (SACs) have emerged as a powerful platform due to their maximal atom utilization efficiency and highly tunable electronic properties[1–4]. However, the intrinsic single-site nature limits their efficacy in complex chemical reactions that require cooperative multi-site interactions[5–10]. To address this challenge, heterogeneous catalytic pairs (CPs) comprising two adjacent active atoms offer a promising solution, which can enable cooperative multiple substrate adsorption/activation, and thereby unlock unconventional reaction pathways[11–14]. For example, heteronuclear Ir_1-P_1 CPs supported on carbon exhibit outstanding hydrogen oxidation activity, arising from the spontaneous H_2 dissociation on Ir and the cooperative $^*H$ desorption by $^*OH$ generated on oxophilic P via spontaneous water dissociation[15]. Similarly, heteronuclear Rb-Ir CPs embedded in a poly(heptazine imide) framework achieve selective photooxidation of glycerol to

[1]Frontiers Science Center for Flexible Electronics (FSCFE) & Institute of Flexible Electronics (IFE), Northwestern Polytechnical University, Xi'an, China. [2]Analytical & Testing Center, Sichuan University, Chengdu, China. [3]Institute for Functional Intelligent Materials, National University of Singapore, Singapore, Singapore. [4]Department of Environmental Science and Engineering, School of Energy and Power Engineering, Xi'an Jiaotong University, Xi'an, China. [5]College of Materials and Energy, Guang'an Institute of Technology, Guang'an, China. [6]Department of Physics, National University of Singapore, Singapore, Singapore. [7]Department of Materials Science and Engineering, City University of Hong Kong, Hong Kong SAR, China. [8]Department of Chemistry, Hong Kong Institute for Clean Energy (HKICE) & Center of Super-Diamond and Advanced Films (COSDAF), City University of Hong Kong, Hong Kong SAR, China. [9]These authors contributed equally: Yiyun Fang, Wen Zhao, Zhilin Xing, Cheng Chen, Xin Zhou. ✉e-mail: iamyyfang@nwpu.edu.cn; iamzqrong@nwpu.edu.cn; phyguon@u.nus.edu; xinzhe.li@xjtu.edu.cn; bliu48@cityu.edu.hk

hydroxypyruvic acid[16]. Despite these advances, homonuclear CPs remain largely unexplored, particularly regarding the impact of inter-CP spacing and coordination asymmetry on their catalytic performance. A fundamental understanding of these factors is critical to unlock the full potential of CPs, enabling enhanced catalytic efficiencies and novel reaction pathways.

In this work, we prepare atomically precise homonuclear Pt_1-Pt_1 CPs with asymmetric Pt_1C_3-$Pt_1O_1C_3$ coordination, anchored on reduced graphene oxide (termed as Pt_1C_3-$Pt_1O_1C_3$/rGO). By finely tuning the inter-distance between the Pt_1C_3-$Pt_1O_1C_3$ CPs to an optimal ~5.3 Å, we achieve a turnover frequency (TOF) of 27,218 h^{-1} for transfer hydrogenation of azobenzene, exceeding benchmarking catalysts by more than an order of magnitude. First-principles calculations reveal that the asymmetric Pt_1C_3-$Pt_1O_1C_3$ CPs separated by a distance of 5.3 Å modulate the electronic structure of the Pt sites, facilitate the co-adsorption of sterically hindered intermediates, and enable an energetically favorable hydrogen shuttling and hydrogenation pathway. These synergistic effects collectively enhance the overall transfer hydrogenation efficiency.

Results and discussion

Synthesis and characterization of Pt_1C_3-$Pt_1O_1C_3$/rGO

The Pt_1C_3-$Pt_1O_1C_3$/rGO catalysts with tunable Pt loadings (0.5–7.5 wt.%) were synthesized by an interface confinement method, leveraging the diatomic structure of the Pt precursor and SiO_2-induced physical confinement[17]. Specifically, the (ethylenediamine)iodoplatinum(II) dimer dinitrate precursor was adsorbed onto graphene oxide (GO), followed by amorphous SiO_2 layer deposition via tetraethyl orthosilicate hydrolysis and thermal treatment. NaOH etching then removed the SiO_2 layer, yielding well-dispersed Pt_1-Pt_1 CPs on rGO. X-ray diffraction (XRD) analysis (Supplementary Fig. 1) confirmed the reduction of GO to rGO, while atomic force microscopy (Supplementary Fig. 2) demonstrated that Pt_1C_3-$Pt_1O_1C_3$/rGO retained a two-dimensional (2D) morphology with atomic thickness.

Aberration-corrected high-angle annular dark-field scanning transmission electron microscope (HAADF-STEM) images (Fig. 1a–j) revealed atomic dispersion of Pt atoms (bright spots) on rGO surface at varying Pt loadings (0.5 wt.%, 1.0 wt.%, 2.5 wt.%, 5.0 wt.%, and 7.5 wt.%, as confirmed by inductively coupled plasma-optical emission spectroscopy), with no observable formation of Pt clusters or nanoparticles (NPs). Magnified HAADF-STEM images (Fig. 1k–o) clearly confirmed the presence of Pt dimers even at low Pt loadings (Fig. 1k), highlighted by solid orange boxes. As the Pt loading increased, the density of Pt dimers correspondingly rose, accompanied by a noticeable reduction in the inter-distance between Pt dimers (the inter-distance is defined as the shortest distance between two Pt atoms from adjacent Pt dimers, namely each Pt atom belongs to a different Pt dimer unit). Notably, the minimal inter-distance between Pt dimers significantly decreased from ~18.1 Å at 0.5 wt.% Pt loading to ~4.6 Å at 7.5 wt.% Pt loading (Fig. 1p–t).

To elucidate the coordination environment of Pt_1-Pt_1 CPs, atomic-resolution electron energy-loss spectroscopy (EELS) and 4D-STEM were performed. EELS measurements of an individual Pt_1-Pt_1 CP simultaneously detected the C-*K*, O-K, and Pt-*M* signals, indicating that Pt atoms are coordinated with both C and O (Fig. 1u–w). Complementary 4D-STEM charge-density mapping revealed two adjacent positively charged Pt centers, each coordinated by negatively charged atoms (Fig. 1x). Strikingly, the coordinating atom adjacent to the lower-left Pt displayed a markedly stronger negative charge density than other Pt-coordinating atoms, consistent with the Pt_1C_3-$Pt_1O_1C_3$ pair owing to the higher electronegativity of O relative to C. In addition, HAADF-STEM images reconstructed from 4D-STEM datasets consistently resolved abundant Pt_1-Pt_1 CPs (Supplementary Fig. 3). A small fraction of isolated single Pt atoms was also observed in the HAADF-STEM images, likely due to pair dissociation or projection overlap in the 2D images[18]. At high Pt loadings (≥8.5 wt.%), small crystalline Pt NPs began to appear (Supplementary Fig. 4)[19]. Energy-dispersive X-ray spectroscopy (EDS) elemental mapping confirmed the homogeneous distribution of C, O, and Pt in the Pt_1C_3-$Pt_1O_1C_3$/rGO catalysts (Fig. 1y).

To examine the electronic property of Pt, X-ray photoelectron spectroscopy (XPS) was performed[20,21]. All Pt_1C_3-$Pt_1O_1C_3$/rGO samples exhibited similar Pt $4f_{7/2}$ and $4f_{5/2}$ peaks at ~73.0 eV and ~76.3 eV, indicating a stable Pt^{2+} oxidation state (Fig. 2a and Supplementary Fig. 5)[22–24]. In contrast, Pt NPs on rGO (Pt_{NPs}/rGO), synthesized via wet-chemical reduction of H_2PtCl_4 (Supplementary Figs. 6 and 7), displayed zero-valent Pt states with Pt $4f_{7/2}$ and $4f_{5/2}$ peaks at 71.4 eV and 74.7 eV, respectively. To further determine the Pt atomic coordination in Pt_1C_3-$Pt_1O_1C_3$/rGO, X-ray absorption spectroscopy (XAS) measurements were conducted. The normalized Pt L_3-edge X-ray absorption near-edge structure (XANES) spectra showed that the white-line of all Pt_1C_3-$Pt_1O_1C_3$/rGO samples was positioned between that of Pt foil and PtO_2 (Fig. 2b), indicating the oxidative state of Pt in Pt_1C_3-$Pt_1O_1C_3$/rGO samples, in good alignment with the XPS results[25]. Fourier-transformed (FT) $k^3\chi(k)$ extended X-ray absorption fine structure (EXAFS) spectra for Pt foil, PtO_2, and Pt_2 precursor revealed dominant peaks at 2.48 Å, 1.68 Å, and 2.45 Å, corresponding to Pt-Pt, Pt-O, and Pt-I first-shell scattering, respectively (Fig. 2c)[26–28]. In contrast, Pt_1C_3-$Pt_1O_1C_3$/rGO samples showed only one prominent peak at around 1.56 Å, which could be attributed to the Pt-C/O first-shell scattering, suggesting that Pt atoms were atomically dispersed on the rGO support, matching well with the HAADF-STEM observations.

To determine the exact atomic structure of Pt_1C_3-$Pt_1O_1C_3$/rGO, we proposed several possible models informed by the above results (Supplementary Fig. 8). The most plausible structure consists of two Pt atoms anchored on adjacent benzene rings in the rGO network (Fig. 2d–f). Specifically, one Pt atom coordinates with three carbon atoms (Pt_1C_3 moiety), while the other coordinates with three carbon atoms and one oxygen atom ($Pt_1O_1C_3$ moiety), forming an asymmetric paired Pt_1C_3-$Pt_1O_1C_3$ configuration. This assignment is corroborated by the charge-density distribution observed in 4D-STEM (Fig. 1x). The average Pt-C/O bond length (approximately 2.11 Å) and the coordination number (around 3.5) of this model agree well with the EXAFS fitting results (Supplementary Table 1). Notably, the average distance between adjacent Pt atoms in a Pt_1C_3-$Pt_1O_1C_3$ pair is approximately 5.0 Å, aligning closely with the statistical data derived from HAADF-STEM imaging. All other proposed structural models failed to replicate the key experimental features, as evidenced by discrepancies in their XANES simulation spectra (Supplementary Fig. 9) and variations in bond lengths and coordination numbers (Supplementary Table 2).

In summary, converging evidence from precursor-directed synthesis, HAADF-STEM, atomic-resolution EELS, 4D-STEM charge-density mapping, electron localization function (ELF) calculation (Supplementary Fig. 10), and XAS, together with XANES simulations and EXAFS fittings, unequivocally establishes the asymmetric Pt_1C_3-$Pt_1O_1C_3$ pair. For clarity, we also present a merged comparison of the atomic structure, 4D-STEM charge-density mapping, and ELF analysis (Supplementary Fig. 11), which supports the proposed Pt_1C_3-$Pt_1O_1C_3$ configuration. Notably, charge-transfer analysis reveals a charge difference of only ~0.07 e^- between the two Pt sites, below the threshold for a detectable XPS shift and consistent with prior reports[15,29]. This is corroborated by ELF calculation and 4D-STEM charge-density mapping results, both of which demonstrate two adjacent Pt centers in comparable charge environments, confirming the persistence of a uniform Pt^{2+} oxidation state in Pt_1C_3-$Pt_1O_1C_3$/rGO.

Hydrogenation of azobenzene

The transfer hydrogenation of azobenzene ($C_6H_5N{=}NC_6H_5$) to hydrazobenzene ($C_6H_5NH\text{-}HNC_6H_5$) via in-situ ammonia borane (NH_3BH_3) hydrolysis was conducted to evaluate the catalytic performance of Pt_1C_3-$Pt_1O_1C_3$/rGO in complex transformations (Fig. 3a). The overall stoichiometric reaction involves one NH_3BH_3 molecule, three

https://doi.org/10.1038/s41467-026-68759-9

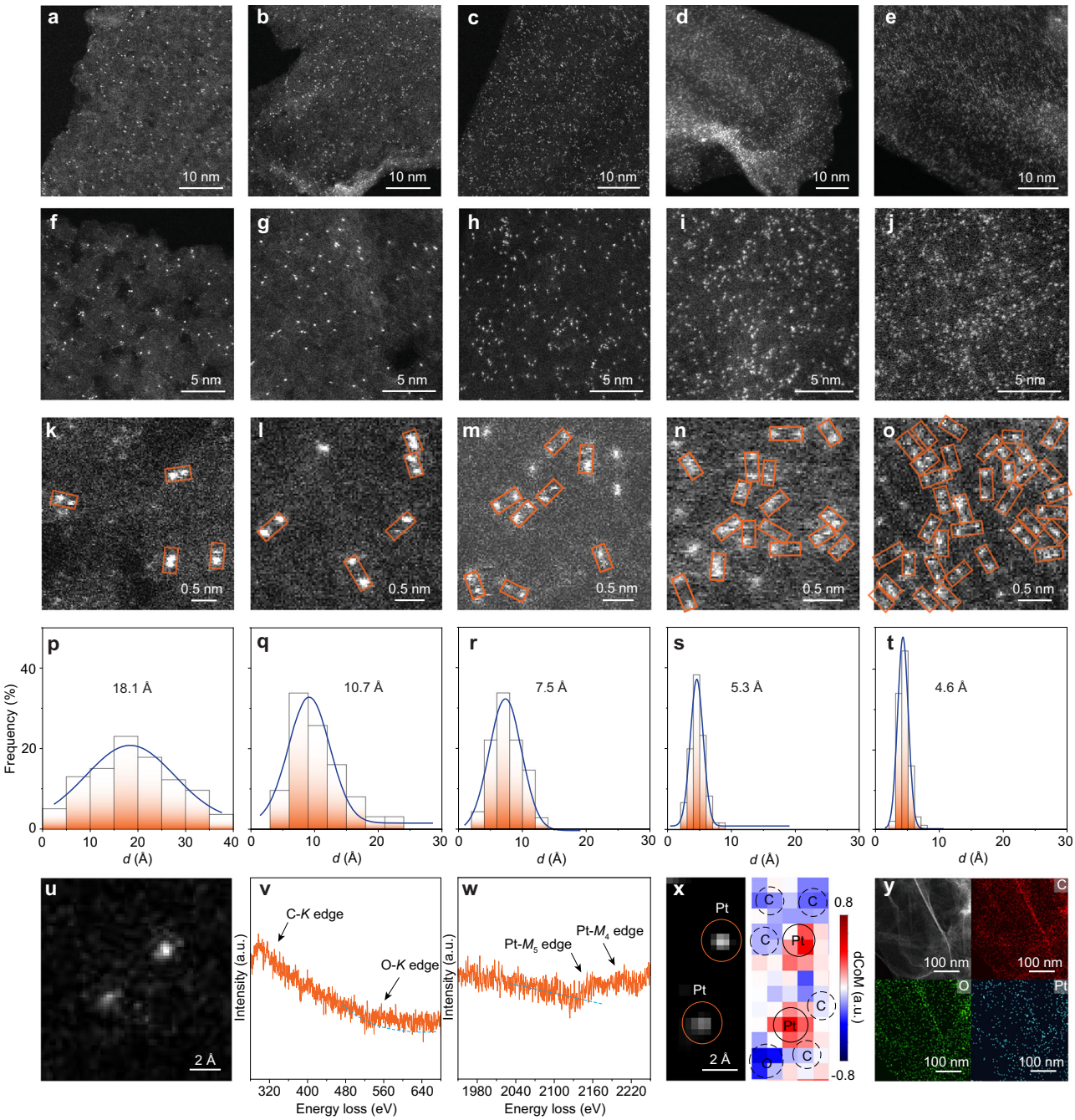

Fig. 1 | Structural characterization of Pt_1C_3-$Pt_1O_1C_3$/rGO samples. Low-magnification HAADF-STEM images of Pt_1C_3-$Pt_1O_1C_3$/rGO with Pt loadings of 0.5 wt.% (**a**), 1.0 wt.% (**b**), 2.5 wt.% (**c**), 5.0 wt.% (**d**), and 7.5 wt.% (**e**). **f**–**j** High-magnification HAADF-STEM images highlighting atomically dispersed Pt sites. **k**–**o** Magnified HAADF-STEM images with orange boxes indicating representative Pt_1C_3-$Pt_1O_1C_3$ pairs. **p**–**t** Statistical distribution of the shortest distances (*d*) between adjacent Pt_1C_3-$Pt_1O_1C_3$ pairs for each sample. **u**–**w** A representative Pt_1-Pt_1 CP on rGO imaged by HAADF-STEM with corresponding EELS spectra. **x** Atomic-scale charge-density mapping by 4D-STEM. Left: HAADF-STEM image reconstructed from the 4D-STEM dataset, resolving a Pt_1-Pt_1 pair on rGO. Right: Projected charge-density distribution derived from the inverted divergence of the center of mass (dCoM), highlighting the spatial positions of C, O, and Pt atoms. **y** EDS mapping of Pt_1C_3-$Pt_1O_1C_3$/rGO catalysts.

$C_6H_5N{=}NC_6H_5$ molecules, and three H_2O molecules, yielding three C_6H_5NH-HNC_6H_5 products[30]. First of all, we optimized the reaction conditions, including solvent, temperature, and reaction time, and revealed methanol as the optimal solvent at a reaction temperature of 80 °C (Supplementary Figs. 12 and 13). As shown in Fig. 3b, at a constant total Pt mass, increasing the Pt loading of Pt_1C_3-$Pt_1O_1C_3$/rGO from 0.5 wt.% to 5.0 wt.% leads to a pronounced enhancement in the yield of C_6H_5NH-HNC_6H_5, rising from 26.6% to as high as 99.8%. However, at a Pt loading of 7.5 wt.%, the yield decreased to 33.6%. It is found that the TOF value strongly depends on the inter-distance between the adjacent Pt_1C_3-$Pt_1O_1C_3$ pairs, peaking at ~5.3 Å with a maximum TOF of $27.2 \times 10^3\,h^{-1}$ (Fig. 3c). On the other hand, both rGO and conventional Pt_{NPs}/rGO (5.0 wt.%) catalysts displayed poor performance in hydrogenation of azobenzene (Fig. 3d). Quantitative comparison of TOF and yield with previously reported catalysts further highlights the superior activity of the Pt_1C_3-$Pt_1O_1C_3$/rGO (Supplementary Table S3). Besides excellent catalytic activity, the Pt_1C_3-$Pt_1O_1C_3$/rGO catalyst also showed outstanding catalytic stability, which could maintain high catalytic

https://doi.org/10.1038/s41467-026-68759-9

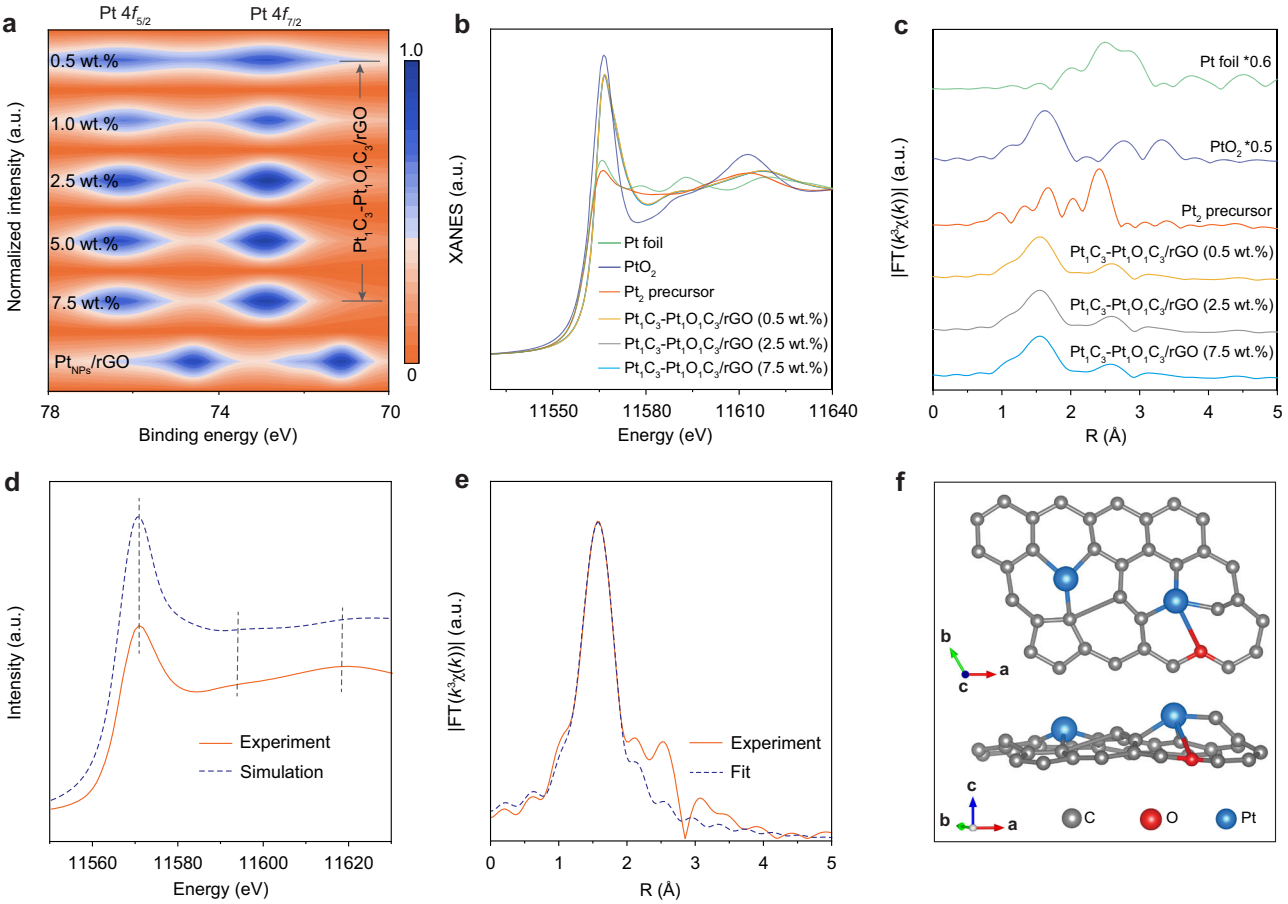

Fig. 2 | XPS, Pt L_3-edge XANES, and EXAFS analysis of Pt_1C_3-$Pt_1O_1C_3$/rGO samples. a XPS spectra of Pt_{NPs}/rGO and Pt_1C_3-$Pt_1O_1C_3$/rGO samples with varying Pt loadings. **b** Pt L_3-edge XANES spectra of Pt foil, PtO_2, and Pt_1C_3-$Pt_1O_1C_3$/rGO samples at 0.5 wt.%, 2.5 wt.%, and 7.5 wt.% Pt loading. **c** FT-EXAFS spectra of Pt foil, PtO_2, and Pt_1C_3-$Pt_1O_1C_3$/rGO samples at 0.5 wt.%, 2.5 wt.%, and 7.5 wt.% Pt loading. **d** Comparison of experimental and simulated XANES spectrum of Pt_1C_3-$Pt_1O_1C_3$/rGO. **e** k^3-weighted FT-EXAFS spectrum of Pt_1C_3-$Pt_1O_1C_3$/rGO with fitting result. **f** The most plausible atomic configuration of Pt_1C_3-$Pt_1O_1C_3$/rGO (black: C, red: O, and blue: Pt).

activity throughout 10 hydrogenation cycles with negligible activity decay (Fig. 3e). The Pt_1C_3-$Pt_1O_1C_3$/rGO morphology was well preserved after 10 cycles of hydrogenation of azobenzene (Supplementary Figs. 14 and 15), highlighting the structural stability of the catalyst.

Besides azobenzene, a broad range of azobenzene derivatives could be hydrogenated via in situ NH_3BH_3 hydrolysis, producing the corresponding products with high efficiency (Fig. 3f). The reaction exhibited excellent tolerance for various substituents, including halogen and alkyl groups at different positions, yielding hydrazobenzene derivatives in remarkable yields (Supplementary Figs. 16–25). This broad applicability highlights the versatility of the Pt_1C_3-$Pt_1O_1C_3$/rGO catalyst for catalyzing the hydrogenation reactions.

Theoretical studies

To provide a deep understanding of the transfer hydrogenation of azobenzene taking place on Pt_1C_3-$Pt_1O_1C_3$, we performed ab initio density functional theory calculations. The Pt_1C_3-$Pt_1O_1C_3$ motif was embedded into four defective graphene supercells to simulate different Pt_1C_3-$Pt_1O_1C_3$/rGO catalysts with varying Pt_1C_3-$Pt_1O_1C_3$ densities. These models, labeled as Models 1-4 (Supplementary Fig. 26), were assigned to the Pt_1C_3-$Pt_1O_1C_3$/rGO catalysts with Pt loading of 1.0 wt.%, 2.5 wt.%, 5.0 wt.%, and 7.5 wt.%, respectively, based on the close agreement between the theoretical inter Pt_1C_3-$Pt_1O_1C_3$ pair spacings and the experimental values obtained from HAADF-STEM (Fig. 1q–t).

We first computed the projected density of states and the *d*-band center for each Pt in Pt_1C_3-$Pt_1O_1C_3$ across different structures (Fig. 4a and Supplementary Fig. 27). At an inter-spacing between adjacent Pt_1C_3-$Pt_1O_1C_3$ pairs of 9.38 Å, both Pt sites show similar *d*-band centers at around −1.11 eV. As the inter-pair distance decreases from 7.24 Å to 5.45 Å, the *d*-band center of Pt_1C_3 increases to −0.04 eV, while that of $Pt_1O_1C_3$ remains at −1.37 eV. At an inter-pair distance of 5.23 Å, this trend reverses, with $Pt_1O_1C_3$ showing a slightly higher *d*-band center (−0.33 eV) than Pt_1C_3 (−0.62 eV). Notably, Model 3 shows a highest *d*-band center of −0.04 eV at the Pt_1C_3 site, indicative of an optimal electronic structure for reactant adsorption[31–33], as confirmed by adsorption energy calculations (Fig. 4b and Supplementary Fig. 28). Specifically, the Pt site with a Pt_1C_3 configuration for Model 3 displays an optimal adsorption energy of −1.53 eV for NH_3BH_3 and −0.43 eV for $C_6H_5N{=}NC_6H_5$. H_2O adsorption is moderate at both sites, indicating that water does not severely compete with the main reactants for Pt sites (Supplementary Table S4).

Further analysis reveals that local structural distortion is the primary cause of varying electronic properties among different models. As shown in Supplementary Fig. 26, the Pt atom in Pt_1C_3 for Model 3 exhibits the greatest protrusion, driven by the balance between Pt density and internal energy. Bader charge and charge differential analyses reveal that 0.3 e^- can be transferred from NH_3BH_3 to Pt_1C_3 (Supplementary Fig. 29), while 0.1 e^- can be transferred from $C_6H_5N{=}NC_6H_5$ to Pt_1C_3 site (Supplementary Fig. 30).

https://doi.org/10.1038/s41467-026-68759-9

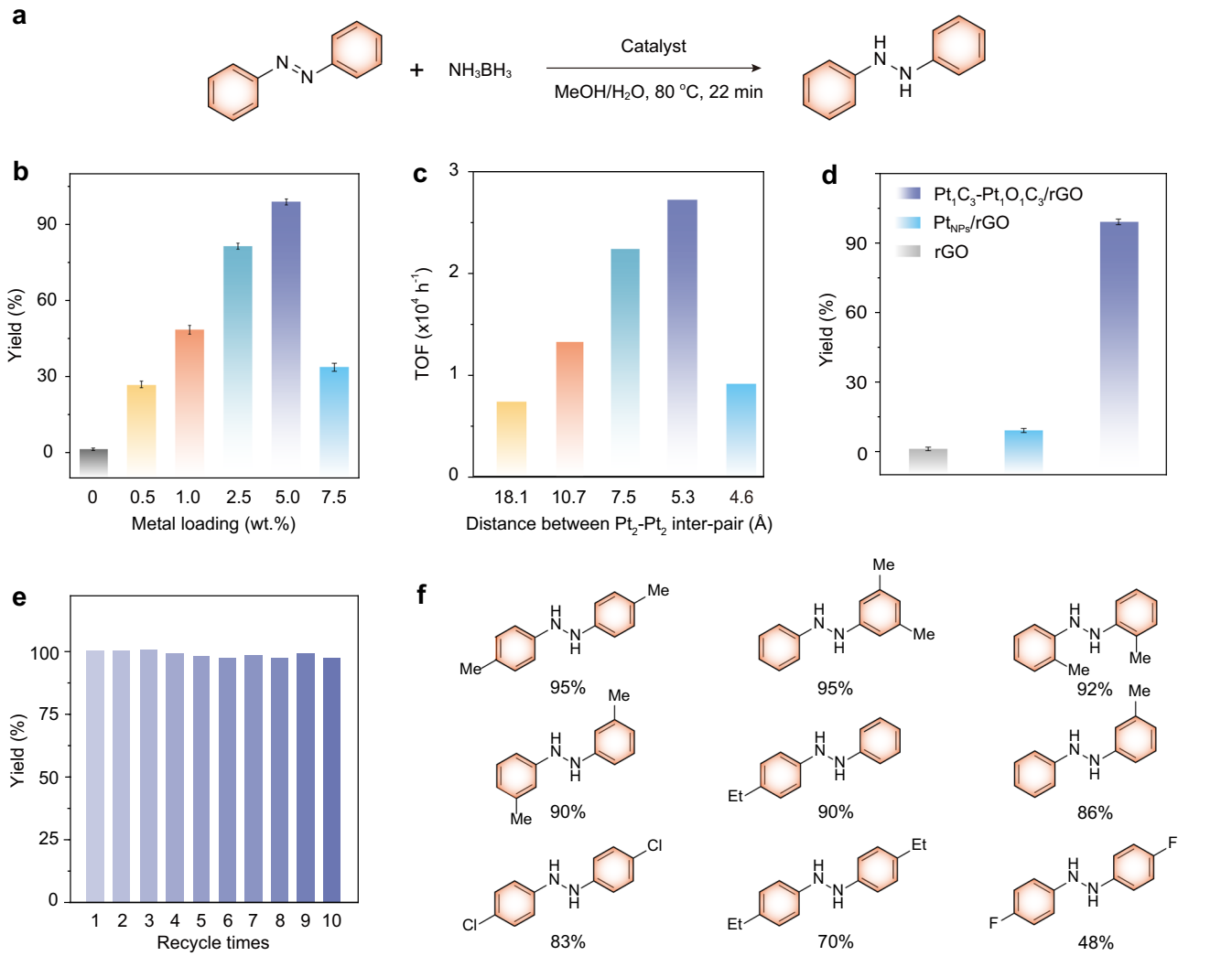

Fig. 3 | Catalytic performance. a Schematic representation of the azobenzene hydrogenation reaction. **b** Catalytic yield of hydrazobenzene as a function of Pt loading in Pt_1C_3-$Pt_1O_1C_3$/rGO. **c** Comparison of TOF values for different Pt_1C_3-$Pt_1O_1C_3$/rGO catalysts with varying inter-pair distances. **d** Yield comparison of Pt_1C_3-$Pt_1O_1C_3$/rGO catalyst (5.0 wt.% Pt) with reference catalysts, including Pt_{NPs}/rGO and rGO, for azobenzene hydrogenation. The error bars in (**b**, **d**) represent the standard deviation of three independent technical replicates ($n = 3$). **e** Stability of Pt_1C_3-$Pt_1O_1C_3$/rGO catalyst (5.0 wt.% Pt) over 10 catalytic cycles, measured under identical reaction conditions. **f** Substrate scope for Pt_1C_3-$Pt_1O_1C_3$/rGO catalyst (5.0 wt.% Pt).

These findings demonstrate that the inter-distance between adjacent Pt_1C_3-$Pt_1O_1C_3$ pairs and the asymmetric PtC_3-PtO_1C_3 configuration can synergistically modulate the electronic properties of Pt sites. The Pt_1C_3-$Pt_1O_1C_3$/rGO catalyst with Model 3 configuration not only offers spatially optimized sites for co-adsorption of sterically hindered $C_6H_5N{=}NC_6H_5$ and NH_3BH_3 (Fig. 4c and Supplementary Fig. 31), but also ensures optimal adsorption strength for these reactants. The azobenzene hydrogenation pathway on Pt_1C_3-$Pt_1O_1C_3$/rGO catalyst with Model 3 configuration was further studied by density functional theory (DFT), which involved the following three key steps (Supplementary Fig. 32): 1. Transfer hydrogenation of $C_6H_5N{=}NC_6H_5$ by NH_3BH_3 hydrolysis, producing one $C_6H_5NHHNC_6H_5$ and leaving $NH_3BH_1^*$ at the Pt_1C_3 site (from co-adsorption to intermediate V). 2. Transfer hydrogenation with $NH_3BH_1^*$ and H_2O to form NH_3BOH^* and a second $C_6H_5NHHNC_6H_5$ (from intermediate VI to XII). 3. Transfer hydrogenation with H_2O as the proton donor to form $NH_3B(OH)_3^*$ and a third $C_6H_5NHHNC_6H_5$ (from intermediate XIII to final desorption). The overall pathway and associated energy barrier are clearly depicted in Fig. 4d, as well as in Supplementary Figs. 33 and 34. Additionally, an alternative pathway was also considered, in which the azo group in azobenzene bonded directly to the Pt_1C_3 site (Supplementary Fig. 35). However, this pathway was energetically unfavorable due to the strong co-adsorption strength and a high energy barrier of 1.08 eV for step III.

The reaction coordinate simulations identified the first H abstraction as the rate-determining step with the highest energy barrier of 1.73 eV (step I). Climbing nudged elastic band (cNEB) simulations further suggested that the first H abstraction process could be broken into two steps by introducing a new H^* intermediate at a neighboring C atom (Supplementary Fig. 36)[34]. By adopting this two-step H abstraction mechanism, initialized with co-adsorption of NH_3BH_3 and $C_6H_5N{=}NC_6H_5$, the first H atom from BH_3 group of NH_3BH_3 transferred to a neighboring C atom to form a new H^* intermediate with an energy barrier of 0.83 eV. Subsequently, the H^* intermediate at the C site was transferred to the Pt atom at the $Pt_1O_1C_3$ site with an energy barrier of 0.90 eV. The reaction barrier heights were predicted to be 1.98 eV and 0.93 eV for TS3 and TS4, respectively. Importantly, NH_3BH_3 hydrolysis was also evaluated on Pt_1C_3-$Pt_1O_1C_3$/rGO with different Pt loadings (Supplementary Table S5), and Model 3 was found to catalyze NH_3BH_3 hydrolysis and generate active H^* intermediates with barriers comparable to those for the first hydrogenation step of azobenzene.

https://doi.org/10.1038/s41467-026-68759-9

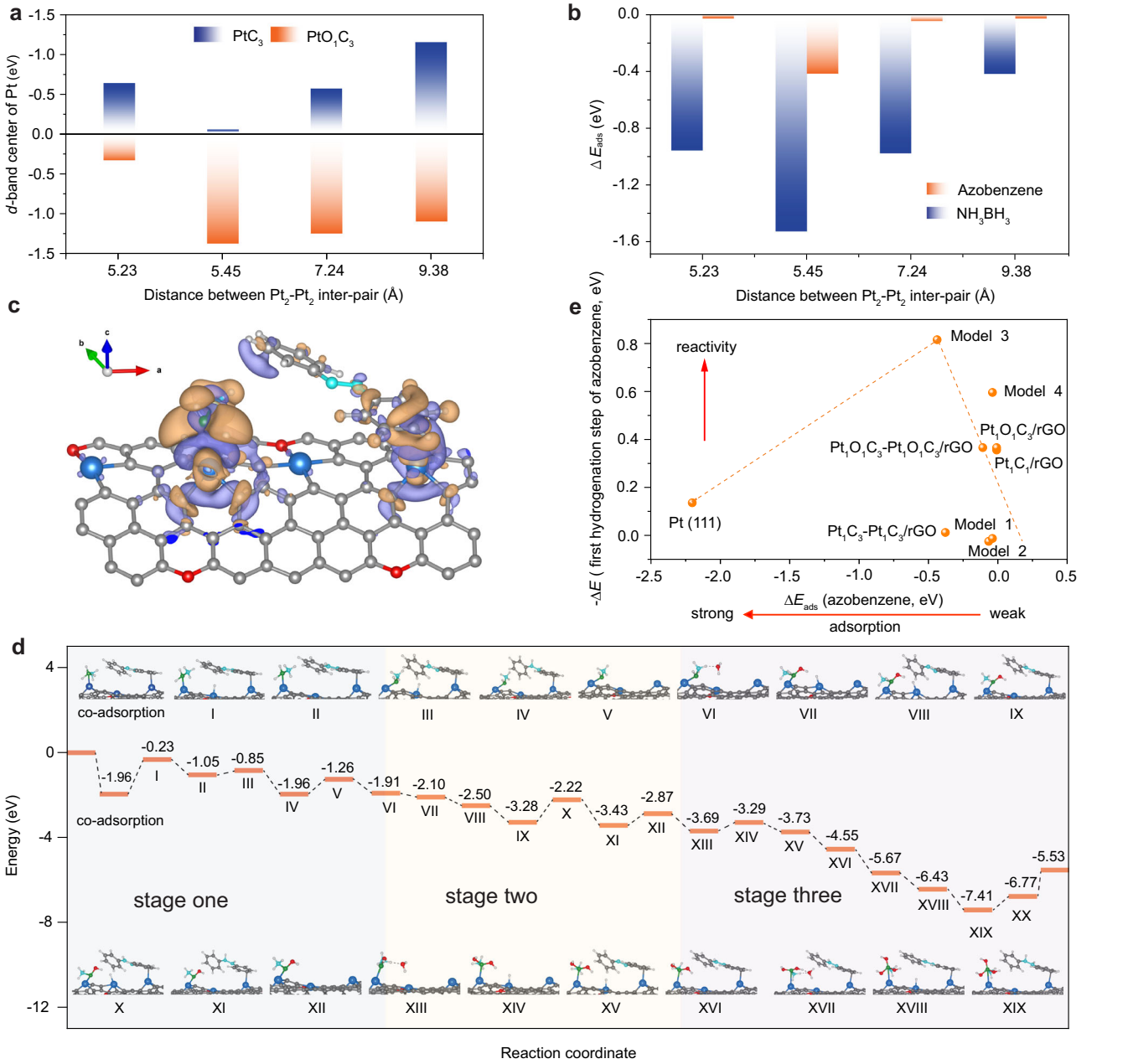

Fig. 4 | Theoretical analysis. a Variation of *d*-band center for Pt sites as a function of inter-pair distance between adjacent Pt_1C_3-$Pt_1O_1C_3$ CPs. **b** Calculated adsorption energies of NH_3BH_3 and $C_6H_5N{=}NC_6H_5$ on Pt_1C_3 as a function of inter-pair distance between adjacent Pt_1C_3-$Pt_1O_1C_3$ CPs. **c** Charge density difference mapping. Orange and purple region indicates charge depletion and charge accumulation, respectively. **d** Reaction pathway and energy profile for hydrogenation of $C_6H_5N{=}NC_6H_5$ to $C_6H_5NHHNC_6H_5$ on Pt_1C_3-$Pt_1O_1C_3$/rGO catalyst with Model 3 configuration. **e** Volcano plot correlating azobenzene adsorption with the reaction energy of the first N=N hydrogenation on various Pt-based catalysts.

Comparatively, we have conducted theoretical calculations on other Pt-based catalysts for transfer hydrogenation of azobenzene, including Pt_1C_3-Pt_1C_3/rGO, $Pt_1O_1C_3$-$Pt_1O_1C_3$/rGO, Pt_1/rGO, and Pt NPs (Supplementary Fig. 37). In Pt_1C_3-Pt_1C_3/rGO, where all Pt sites adopt the symmetric Pt_1C_3 configuration, and the dissociated H atoms bind strongly to the Pt sites, with an adsorption energy of −8.26 eV (Supplementary Fig. 38). This strong binding inhibits H-atom transfer, making Pt_1C_3-Pt_1C_3/rGO ineffective for hydrogenating $C_6H_5N{=}NC_6H_5$. $Pt_1O_1C_3$-$Pt_1O_1C_3$/rGO exhibits universally weak adsorption for azobenzene, NH_3BH_3, and H_2O (Supplementary Table S6). Pt_1/rGO with $Pt_1O_1C_3$ configuration exhibits weak binding to NH_3BH_3, with an adsorption energy of −0.15 eV (Supplementary Fig. 39). Pt NPs are suboptimal due to the excessive adsorption strength of NH_3BH_3 (−2.16 eV) and $C_6H_5N{=}NC_6H_5$ (−2.20 eV) (Supplementary Fig. 40), leading to catalyst poisoning. We further established a volcano relationship by correlating ΔE_{ads}(azobenzene) with the reaction energy of the first N=N hydrogenation for various models (Fig. 4e). In this plot, Pt (111) resides on the over-binding branch, whereas Pt_1C_3-$Pt_1O_1C_3$/rGO (Models 1, 2, and 4), $Pt_1O_1C_3$-$Pt_1O_1C_3$/rGO, Pt_1C_3/rGO, and $Pt_1O_1C_3$/rGO fall on the weak-binding branch. The first hydrogenation of azobenzene becomes energetically disfavored for Pt_1C_3-Pt_1C_3/rGO. By contrast, the Pt_1C_3-$Pt_1O_1C_3$/rGO (Model 3) sits at the apex of the volcano plot, exhibiting a balanced adsorption strength coupled

with the lowest reaction energy for the first hydrogenation step. These calculation results highlight the crucial asymmetric paired PtC_3-PtO_1C_3 configuration with an optimized inter-pair spacing, which can effectively promote the transfer hydrogenation of azobenzene.

Discussion

In summary, we have successfully prepared atomically dispersed asymmetric Pt_1C_3-$Pt_1O_1C_3$ CPs anchored on rGO. By precisely tuning the inter-spacing between the adjacent Pt_1C_3-$Pt_1O_1C_3$ CPs to approximately 5.3 Å, the Pt_1C_3-$Pt_1O_1C_3$/rGO catalyst achieves an optimal performance in transfer hydrogenation of azobenzene via ammonia-borane hydrolysis. The Pt_1C_3-$Pt_1O_1C_3$ CPs separated by 5.3 Å precisely modulate the local electronic environment of each Pt site and enable the co-adsorption of sterically hindered $C_6H_5N{=}NC_6H_5$ and NH_3BH_3 molecules. Furthermore, the unique asymmetric paired Pt_1C_3-$Pt_1O_1C_3$ configuration facilitates hydrogen abstraction and transfer. Our work provides a deeper understanding of the structure-performance relationship in CPs and opens new avenues for rationally designing advanced catalysts for highly efficient chemical transformations.

Methods

Materials

(Ethylenediamine)iodoplatinum(II) dimer dinitrate (96%, Sigma-Aldrich), chloroplatinic acid hexahydrate ($H_2PtCl_6{\cdot}6H_2O$, 99.9%, Adamas), graphene oxide (GO, 0.5–5 μm, XFNANO), tetraethyl orthosilicate (TEOS, SiO_2 > 28.4%, Sigma-Aldrich), ammonia solution (25–28%, Sigma-Aldrich), sodium hydroxide (NaOH, 98%, Aladdin), sodium borohydride ($NaBH_4$, 98%, Energy chemical), azobenzene (97%, Macklin), borane-ammonia complex (NH_3BH_3, 97%, Macklin), and other reagents were purchased from commercial suppliers and used without further purification.

Synthesis of Pt_1C_3-$Pt_1O_1C_3$/rGO catalysts

One hundred milligrams of GO was dispersed in 50 mL of deionized water through sonication, followed by the addition of 200 mL of ethanol. A specific amount of Pt_2 precursor was dispersed in 10 mL of ethanol and subsequently added to the GO ethanol solution. The mixture was stirred at room temperature for 12 h. The TEOS (2.75 mL in 25 mL ethanol) was then added dropwise to the mixture and stirred for an additional 13 h. The resulting product was centrifuged, washed thoroughly with water and ethanol, and dried under vacuum. The dried powder was calcined at 400 °C under N_2 atmosphere for 2 h. Finally, silicon species in the sample were removed by etching with 3 M NaOH solution at room temperature for 3 h, yielding the final Pt_1C_3-$Pt_1O_1C_3$/rGO catalyst. The Pt loading in the Pt_1C_3-$Pt_1O_1C_3$/rGO catalyst was controlled by varying the amount of Pt_2 precursor used in the synthesis. The Pt loadings in catalysts were confirmed by inductively coupled plasma-optical emission spectroscopy.

Synthesis of Pt_{NPs}/rGO catalysts

Pt_{NPs}/rGO catalysts were synthesized using a procedure similar to that of Pt_1C_3-$Pt_1O_1C_3$/rGO, with $H_2PtCl_6{\cdot}6H_2O$ as the Pt precursor and $NaBH_4$ as the reducing agent. Specifically, an amount of $H_2PtCl_6{\cdot}6H_2O$ was dispersed in 10 mL of ethanol and subsequently added to the ethanol solution containing GO. The mixture was stirred at room temperature for 13 h, followed by the addition of $NaBH_4$ as the reducing agent. The subsequent steps, including washing, drying, calcination, and etching with 3 M NaOH to remove silicon species, were identical to those used for Pt_1C_3-$Pt_1O_1C_3$/rGO synthesis. The final product was denoted as Pt_{NPs}/rGO.

The hydrogenation reactions

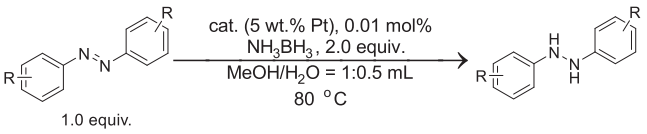

Reaction conditions for azobenzene and derivative hydrogenation

In an oven-dried 10 mL Schlenk tube equipped with a magnetic stir bar, azobenzene (0.2 mmol) and ammonia borane (0.4 mmol) were sequentially added. The tube was sealed with a rubber septum, evacuated, and refilled with N_2 gas. Then, 0.01 mol.% Pt_1C_3-$Pt_1O_1C_3$/rGO catalyst was introduced. For example, in the case of Pt_1C_3-$Pt_1O_1C_3$/rGO (5 wt.%), 8 mg of catalyst was ultrasonically dispersed in 50 mL of deionized water, and 0.5 mL of this dispersion, together with 1 mL of solvent (typically methanol), was transferred into the reaction tube. A nitrogen balloon was attached as shown in Supplementary Fig. 41.

The mixture was stirred at 80 °C for 22 min, then cooled to room temperature. The catalyst was separated by centrifugation, washed twice with ethyl acetate (2 × 5 mL), and the combined filtrate was dried over anhydrous Na_2SO_4. After filtration, the solvent was removed under reduced pressure at 40 °C using a rotary evaporator. The residue was dissolved in deuterated chloroform ($CDCl_3$), and 1,1,2,2-tetrachloroethane (TCE) was added as an internal standard for nuclear magnetic resonance (NMR) analysis. Optimization studies of solvent, temperature, and time identified methanol at 80 °C as the optimal condition (Supplementary Figs. 12 and 13). Reactions involving substituted azobenzene derivatives were performed under identical conditions except that the reaction time was extended to 120 min. The crude products were purified by flash column chromatography on silica gel using hexane/ethyl acetate as the eluent to yield the corresponding hydrogenated products.

Catalytic performance evaluation

Catalytic performance was quantified using azobenzene hydrogenation over the Pt_1C_3-$Pt_1O_1C_3$/rGO (5 wt.%) catalyst as a representative case. Product yields were determined from NMR data according to Eq. (1):

$$\begin{aligned}\text{Yield}(\%) &= \frac{n(\text{obtained products})}{n(\text{initally added substrates})} \\ &= \frac{\frac{m_{TCE}\times 2\times 2.6}{M_{TCE}\times 4}}{n(\text{initally added substrates})} \\ &= \frac{\frac{25.75\text{mg}\times 2\times 2.60}{167.85\text{g/mol}\times 4}}{0.2\text{mmol}} = 99.8\%\end{aligned} \tag{1}$$

The conversion and selectivity were calculated according to Eqs. (2) and (3), respectively:

$$\begin{aligned}\text{Conversion}(\%) &= \left[1-\frac{n(\text{remained substrate})}{n(\text{initial substrate}}\right]\times 100\% \\ &= (1-0)=100\%\end{aligned} \tag{2}$$

$$\begin{aligned}\text{Selectivity}(\%) &= \frac{n(\text{obtained product})}{n(\text{initial substrate})-n(\text{remained substrate})}\times 100\% \\ &= \frac{\frac{m_{TCE}\times 2\times 2.6}{M_{TCE}\times 4}}{n(\text{initial substrate})-n(\text{remained substrate})} \\ &= \frac{\frac{25.75\text{mg}\times 2\times 2.60}{167.85\frac{\text{g}}{\text{mol}}\times 4}}{0.2\text{mmol}-0} = 99.8\%\end{aligned} \tag{3}$$

The turnover frequency (TOF) was calculated at the 22-min time point from NMR spectra according to Eq. (4):

$$\begin{aligned} \mathrm{TOF} &= \frac{\text{moles of reactant converted}}{\text{mole of total active sites} \times \text{reaction time}} \\ &= \frac{\text{amount of azobenzene(mol)} \times \text{conversion(\%)} \times \text{selectivity(\%)}}{\text{amount of catalyst(mol)} \times \text{reaction time(h)}} \\ &= \frac{0.2\text{mmol} \times 100\% \times 99.8\%}{0.0002\text{mmol} \times 0.367\text{h}} = 27218\ \mathrm{h}^{-1} \end{aligned} \quad (4)$$

Characterization

Wide-angle X-ray diffraction (XRD) patterns were collected on a Bruker D8 Focus Powder X-ray diffractometer using Cu Kα radiation (40 kV, 40 mA) at room temperature. Aberration-corrected high-annular dark-field scanning transmission electron microscopy (HAADF-STEM) and energy-dispersive X-ray spectroscopy (EDS) mappings were collected on an aberration-corrected Thermo Fisher Spectra 300 system equipped with a cold field emission gun and an ASCOR probe corrector at 300 kV. The metal loadings in all the samples were measured by inductively coupled plasma-optical emission spectroscopy (Perkin Elmer Avio 500, UK). Atomic force microscopy (AFM) topography measurements were performed with an XE-100 AFM (Park Systems) in noncontact mode. The X-ray absorption near-edge structure (XANES) and the extended X-ray absorption fine structure (EXAFS) measurements of Pt L_3-edge were carried out at the beamline of the Singapore synchrotron light source. Pt foil was used for the energy calibration, and all samples were measured under transmission mode at room temperature. Si (111) double crystal monochromator was used to filter the X-ray beam. EXAFS oscillations χ(k) were extracted and analyzed using the Demeter software package. Energy-loss spectroscopy (EELS) spectrum imaging was conducted using a Gatan Quantum ER spectrometer with an exposure time of 2 ms per pixel. Four-dimensional (4D) STEM datasets were acquired on a JEOL ARM200F microscope equipped with an ASCOR aberration corrector and a Merlin Medipix3 1 R pixelated detector (256 × 256 pixels, 6-bit depth), with a convergence semi-angle of approximately 21 mrad. Charge-density mapping was carried out via Gauss's law by computing the divergence of the inverted electric-field distribution reconstructed from the 4D-STEM datasets using the open-source LiberTEM software[35]. To minimize long-range background features, a Gaussian filter with a kernel size of two pixels was applied[36].

Theoretical calculations

The spin-polarized density functional theory (DFT) calculations were performed utilizing the Vienna Ab Initio Simulation Package (VASP, version 5.4.4)[37,38]. The generalized gradient approximation in the Perdew-Burke-Ernzerh format and the plane wave basis kinetic energy cutoff of 500 eV were used in all calculations[39,40]. The structural relaxations were carried out until the Hellmann-Feynman force on each atom was less than 0.01 eV/Å, and the energy convergence criterion was set to 10^{-4} eV. The gamma point sampling in the Brillouin zone was employed in all calculations. Along the direction perpendicular to the 2D graphene substrate sheet, a vacuum of 15 Å is included in the supercell to avoid the interaction of neighboring images. The reaction barrier was determined by the climbing-image nudged elastic band method[34].

Data availability

The data that support the findings of this study are reported within the Article and its Supplementary Information and are available from the corresponding author upon request. Source data are provided with this paper.

References

1. Qiao, B. et al. Single-atom catalysis of CO oxidation using Pt_1/FeO_x. *Nat. Chem.* **3**, 634–641 (2011).
2. Xu, H., Cheng, D., Cao, D. & Zeng, X. Revisiting the universal principle for the rational design of single-atom electrocatalysts. *Nat. Catal.* **7**, 207–218 (2024).
3. Wu, G. & Zelenay, P. Activity versus stability of atomically dispersed transition-metal electrocatalysts. *Nat. Rev. Mater.* **9**, 643–656 (2024).
4. Chang, J. et al. Synthesis of ultrahigh-metal-density single-atom catalysts via metal sulfide-mediated atomic trapping. *Nat. Synth.* **3**, 1427–1438 (2024).
5. Guo, Y., Wang, M., Zhu, Q., Xiao, D. & Ma, D. Ensemble effect for single-atom, small cluster and nanoparticle catalysts. *Nat. Catal.* **5**, 766–776 (2022).
6. Jia, C. et al. Challenges and opportunities for single-atom electrocatalysts: from lab-scale research to potential industry-level applications. *Adv. Mater.* **36**, 2404659 (2024).
7. Dong, C. et al. Fully exposed palladium cluster catalysts enable hydrogen production from nitrogen heterocycles. *Nat. Catal.* **5**, 485–493 (2022).
8. Chen, X. et al. Regulating coordination number in atomically dispersed Pt species on defect-rich graphene for n-butane dehydrogenation reaction. *Nat. Commun.* **12**, 2664 (2021).
9. Lv, D. et al. Dual spatial and electronic regulation in van der Waals Cu_3Se_2 nanosheets for electrocatalytic acetylene semi-hydrogenation. *Angew. Chem. Int. Ed.* **64**, e202516180 (2025).
10. Tang, S. et al. Electrochemical alkyne semi-hydrogenation via proton-coupled electron transfer on Cu(111) surface. *Angew. Chem. Int. Ed.* **64**, e202510192 (2025).
11. Wang, Q., Cheng, Y., Yang, H. B., Su, C. & Liu, B. Integrative catalytic pairs for efficient multi-intermediate catalysis. *Nat. Nanotechnol.* **19**, 1442–1451 (2024).
12. Ding, J. et al. Circumventing CO_2 reduction scaling relations over the heteronuclear diatomic catalytic pair. *J. Am. Chem. Soc.* **145**, 11829–11836 (2023).
13. Ni, J. et al. Atomic Co-P catalytic pair drives efficient electrochemical nitrate reduction to ammonia. *Adv. Energy Mater.* **14**, 2400065 (2024).
14. Fan, Y. et al. Asymmetric Ru-In atomic pairs promote highly active and stable acetylene hydrochlorination. *Nat. Commun.* **15**, 6035 (2024).
15. Wang, Q. et al. Atomic metal-non-metal catalytic pair drives efficient hydrogen oxidation catalysis in fuel cells. *Nat. Catal.* **6**, 916–926 (2023).
16. Teng, Z. et al. Asymmetric photooxidation of glycerol to hydroxypyruvic acid over Rb-Ir catalytic pairs on poly(heptazine imides). *Nat. Nanotechnol.* **20**, 815–824 (2025).
17. Li, X. et al. Atomically precise single metal oxide cluster catalyst with oxygen-controlled activity. *Adv. Funct. Mater.* **32**, 2200933 (2022).
18. Li, X. et al. Advances in heterogeneous single-cluster catalysis. *Nat. Rev. Chem.* **7**, 754–767 (2023).
19. Peng, B. et al. Embedded oxide clusters stabilize sub-2 nm Pt nanoparticles for highly durable fuel cells. *Nat. Catal.* **7**, 818–828 (2024).
20. Niu, W. et al. Reaction-driven restructuring of defective $PtSe_2$ into ultrastable catalyst for the oxygen reduction reaction. *Nat. Mater.* **23**, 1704–1711 (2024).
21. Shao, G. et al. Dynamic coordination engineering of 2D $PhenPtCl_2$ nanosheets for superior hydrogen evolution. *Nat. Commun.* **15**, 385 (2024).
22. Chen, J. et al. Diversity of platinum-sites at platinum/fullerene interface accelerates alkaline hydrogen evolution. *Nat. Commun.* **14**, 1711 (2023).
23. Meng, X.-Y. et al. Long-term stable hydrogen production from water and lactic acid via visible-light-driven photocatalysis in a porous microreactor. *Angew. Chem. Int. Ed.* **62**, e202307490 (2023).

24. Zhao, W. et al. Triggering Pt active sites in basal plane of van der Waals $PtTe_2$ materials by amorphization engineering for hydrogen evolution. *Adv. Mater.* **35**, 2301593 (2023).
25. Du, Y. et al. XAFCA: a new XAFS beamline for catalysis research. *J. Synchrotron Radiat.* **22**, 839–843 (2015).
26. Zeng, L. et al. Anti-dissolution Pt single site with $Pt(OH)(O_3)/Co(P)$ coordination for efficient alkaline water splitting electrolyzer. *Nat. Commun.* **13**, 3822 (2022).
27. Li, X. et al. Ordered clustering of single atomic Te vacancies in atomically thin $PtTe_2$ promotes hydrogen evolution catalysis. *Nat. Commun.* **12**, 2351 (2021).
28. Liu, S., Wang, Y., Lyu, K. F., Lan, X. & Wang, T. A one-pot strategy for anchoring single Pt atoms in MOFs with diverse coordination environments. *Nat. Synth.* **3**, 1158–1167 (2024).
29. Chen, G. et al. Precisely tailoring the second coordination sphere of a cobalt single-atom catalyst for the selective hydrogenation of halogenated nitroarenes. *Angew. Chem. Int. Ed.* **64**, e202421277 (2025).
30. Wang, F., Planas, O. & Cornella, J. Bi(I)-catalyzed transfer-hydrogenation with ammonia-borane. *J. Am. Chem. Soc.* **141**, 4235–4240 (2019).
31. Wang, J., Zhang, Y., Jiang, S., Sun, C. & Song, S. Regulation of *d*-band centers in localized CdS homojunctions through facet control for improved photocatalytic water splitting. *Angew. Chem. Int. Ed.* **62**, e202307808 (2023).
32. Liu, H.-Z. et al. Tailoring d-band center of high-valent metal-oxo species for pollutant removal via complete polymerization. *Nat. Commun.* **15**, 2327 (2024).
33. Xing, Z. et al. Disordered Cu sites in amorphous Cu_2Te nanosheets promote electrocatalytic acetylene semi-hydrogenation. *Adv. Mater.* **37**, 2510774 (2025).
34. Henkelman, G., Uberuaga, B. P. & Jónsson, H. A climbing image nudged elastic band method for finding saddle points and minimum energy paths. *J. Chem. Phys.* **113**, 9901–9904 (2000).
35. Clausen, A. et al. LiberTEM: software platform for scalable multi-dimensional data processing in transmission electron microscopy. *J. Open Source Softw.* **5**, 2006 (2020).
36. Zachman, M. J. et al. Measuring and directing charge transfer in heterogenous catalysts. *Nat. Commun.* **13**, 3253 (2022).
37. Kresse, G. & Hafner, J. Ab initio molecular-dynamics simulation of the liquid-metal-amorphous-semiconductor transition in germanium. *Phys. Rev. B* **49**, 14251–14269 (1994).
38. Kresse, G. & Furthmüller, J. Efficient iterative schemes for ab initio total-energy calculations using a plane-wave basis set. *Phys. Rev. B* **54**, 11169–11186 (1996).
39. Perdew, J. P., Burke, K. & Ernzerhof, M. Generalized gradient approximation made simple. *Phys. Rev. Lett.* **77**, 3865–3868 (1996).
40. Kresse, G. & Joubert, D. From ultrasoft pseudopotentials to the projector augmented-wave method. *Phys. Rev. B* **59**, 1758–1775 (1999).

Acknowledgements

The work was supported by the Natural Science Foundation of China (22471218 to Z.-Q.R.; 22305184 and 22576162 to X.Z.L.; 22204111 to C.C.), National Defense Basic Scientific Research Program of China (JCKY2022607C007 to Y.Y. F.), Natural Science Foundation of Shaanxi Province (2023-JC-QN-0136 to X.Z.L.; 2025JC-YBMS-147 to Y.Y.F.), Shaanxi Fundamental Science Research Project for Chemistry & Biology (22JHQ002 Z.-Q.R.), the Program for Young Talents of Shaanxi Province (5113190023 to Z.-Q.R.), Natural Science Basic Research Program of Shaanxi (2024JC-ZDXM-08 to Z.-Q.R.), Natural Science Foundation of Zhejiang Province(LY24B010002 to Y.Y.F.), the Innovation Foundation for Doctor Dissertation of Northwestern Polytechnical University (CX2024106 to W.Z.), the City University of Hong Kong startup fund (9020003 to B.L.), ITF-RTH- Global STEM Professorship (9446006 to B.L.) and JC STEM lab of Advanced CO_2 Upcycling (9228005 to B.L.). Computations were performed using the NUS High Performance Computing (HPC) facilities and the National Supercomputing Centre (NSCC) in Singapore. We also thank Shibo Xi from the Institute of Chemical and Engineering Sciences, Singapore, for conducting and analyzing the XANES and EXAFS measurements.

Author contributions

Y.Y.F., Z.-Q.R., N.G., X.Z.L., and B.L. conceived the research. X.Z.L., Y.Y.F., W.Z., and Z.L.X. carried out the synthesis and materials characterization and measurements. N.G. conducted the theoretical calculation. C.C. performed the HAADF-STEM measurement. X.Z. performed the EELS and 4D-STEM measurement and analysis. C.C.C., X.C.W., S.M.Z., Q.Y.L., D.D.L., S.Q.L., and Z.H.C. assisted in the synthesis and characterization of materials. X.Z.L., B.L., Y.Y.F., W.Z., N.G., Z.-Q.R., X.Z., and Z.L.X. wrote the manuscript. All authors discussed the results and commented on the manuscript.

Competing interests

The authors declare no competing interests.

Additional information

Supplementary information The online version contains supplementary material available at https://doi.org/10.1038/s41467-026-68759-9.

Correspondence and requests for materials should be addressed to Yiyun Fang, Zi-Qiang Rong, Na Guo, Xinzhe Li or Bin Liu.

Peer review information *Nature Communications* thanks Ji Hoon Shim and the other, anonymous, reviewer(s) for their contribution to the peer review of this work. A peer review file is available.